UAV Icing: Ice Shedding Detection Methods for an Electrothermal De-Icing System

Bogdan Løw-Hansen*

Norwegian University of Science and Technology, NTNU, 7491, Trondheim, Norway

Richard Hann†

Norwegian University of Science and Technology, NTNU, 7491, Trondheim, Norway and
UBIQ Aerospace, 7011, Trondheim, Norway

Tor Arne Johansen‡

Norwegian University of Science and Technology, NTNU, 7491, Trondheim, Norway

Among the identified problems with unmanned aerial vehicles (UAVs), especially with the medium-sized fixed-wing UAVs, is a lack of mature ice protection systems (IPSs). One of the emerging UAV ice protection technologies is based on electrothermal de-icing, where heating elements are integrated into the wings of a UAV. In icing conditions, this allows the UAV wings to be heated, resulting in weakened ice adhesion and subsequent ice shedding. A drawback of such de-icing system is that it requires substantial amounts of energy. This study addresses the issue of energy consumption by proposing two electrothermal ice shedding detection algorithms that make it possible for a de-icing system to be turned off shortly after ice shedding has occurred. This is in contrast to fixed de-icing periods where the heating elements operate irrespective of the ice shedding status. The first proposed algorithm is based on parameter change detection, which involves thresholding the innovation sequence of a first-order temperature-estimating Kalman filter (KF). The second algorithm is based on pattern matching using the continuous wavelet transform (CWT) of the KF innovation sequence. The results, based on icing wind tunnel experiments, show that both approaches can produce accurate detections with an F-measure of 1.0 and average detection times of 1.98 seconds and 2.53 seconds, respectively. Thus, making it possible to optimize the efficiency of electrothermal IPSs.

I. Introduction

RESEARCH on in-flight icing for unmanned aerial vehicles (UAVs) is a new topic that has only recently started to gain momentum [1]. Small to medium fixed-wing UAVs, with a wingspan of a couple of meters, are currently considered to have significant potential to succeed in many commercial applications [2]. Moreover, improving the UAV technology is also highly relevant now as UAVs have recently shown to be extremely valuable for critical missions such as search and rescue, human organ transport, and surveillance missions [3, 4]. For many of these use-cases, the UAVs have to be able to operate in adverse weather conditions, including atmospheric icing, which is considered to be one of the main challenges when trying to build all-weather-capable UAVs [1].

This study aims to contribute to the design of ice protection systems (IPSs) that can ensure the safe operation of UAVs in atmospheric icing conditions. The importance of this research stems from the fact that atmospheric icing is recognized as a severe hazard for UAVs that can lead to issues ranging from reduced flight performance to complete loss of lift and control of the UAV, as demonstrated in the performance degradation study by Hann and Johansen [5]. Furthermore, the extent of the icing issue is partly captured in the results of the climate report on atmospheric icing by Sørensen et al. [6]. The report states that in cold climate regions, such as northern Europe, atmospheric icing is likely to be a concern for typical fixed-wing UAVs, in some cases reducing their potential operational window by more than 50% depending on the specific time and location. Moreover, the icing climatology report by Bernstein et al. [7, 8] shows that

---

*PhD-candidate, Center for Autonomous Marine Operations and System, NTNU, Department of Engineering Cybernetics, bogdan.l.hansen@ntnu.no, AIAA Student Member

†Researcher, Center for Autonomous Marine Operations and System, NTNU, Department of Engineering Cybernetics, richard.hann@ntnu.no, AIAA Member

‡Professor, Center for Autonomous Marine Operations and System, NTNU, Department of Engineering Cybernetics, tor.arne.johansen@ntnu.no

icing conditions can occur almost anywhere in the world, making the problem of icing relevant for a substantial number of UAV operations.

The issue researched in this study concerns the energy optimization of an electrothermal de-icing system. The specific de-icing system used to tune and showcase the developed detection algorithms is based on the UBIQ[§] D•ICE technology. The de-icing system provided by UBIQ relies on electrically heated carbon-fiber layers and thermal sensors built into the UAV wings, with a layout as shown in Fig. 1 [9]. The system operates by heating the UAV wings when in icing conditions. This weakens the adhesive force that holds the ice to the airframe and allows the aerodynamic forces to shed off the accreted ice, as shown in Fig. 2.
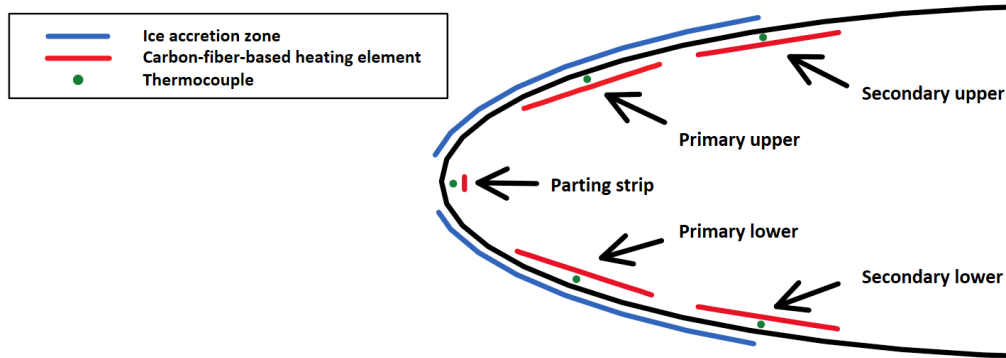

Fig. 1   Cross-section schematic of the built-in de-icing IPS. The UAV wing embeds four periodically heated electrothermal carbon fiber layers, one continuously heated wire across the leading edge (the parting strip) and five corresponding thermocouples.
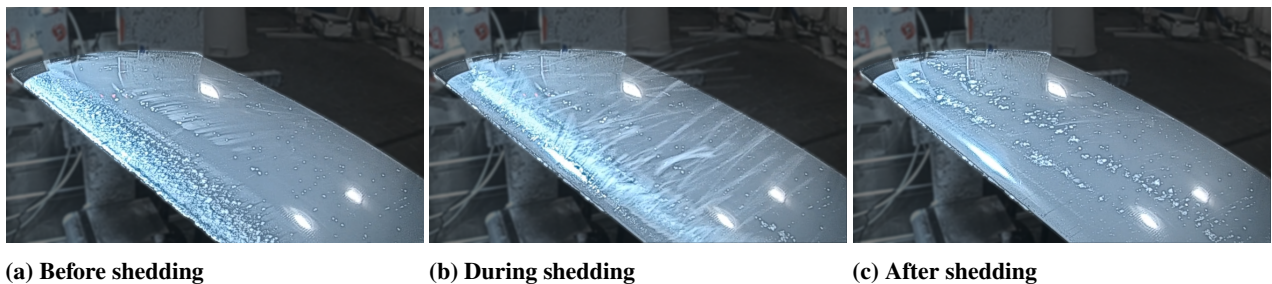

(a) Before shedding   **(b) During shedding**   **(c) After shedding**

Fig. 2   The ice shedding process: before, during and after. Photo: Richard Hann.

Depending on the heating regime, a de-icing IPS with five heating elements, as shown in Fig. 1, can exceed 20 kW/m^2 consumption when active at $-10\,°C$. The expected operation interval of the system at 25 m/s wind and 0.45 g/m^3 liquid water content (LWC) is 25 seconds, as reported by Wallisch and Hann in [10]. Moreover, with the expected ice shedding time of 12 seconds, also reported in [10], it is evident that a fast and precise ice shedding detection system would be able to substantially reduce the overall energy needs of the described IPS.

In general, ice shedding detection is a secondary function of an IPS. Therefore, even though not much research has been done on ice shedding detection specifically, several articles have already been published on the development and use of electrothermal IPSs, and modeling of the ice shedding phenomena. Early prototypes of the IPS developed by UBIQ are presented by Sørensen et al. in [11] and tested using real UAV flight data in [12]. Additional testing of the IPS system has also been performed by Hann et al. in [13], where it was used to detect icing conditions. In [14] R. Henry presents an electrothermal icing/de-icing model; the model is based on the 2D heat equation and can be used to predict the icing state of a UAV airframe and thereby predict ice shedding. A similar modeling approach, but with a 3D heat equation, is used by Lei et al. in [15] to develop a new melting model for an electrothermal de-icing simulator. Additionally, the mechanics of ice shedding are examined by Enache et al. in [16], where ice melting and shedding experiments are both simulated and then validated through icing wind tunnel experiments.

[§]UBIQ Aerospace, a start-up company that develops IPSs for UAVs. https://www.ubiqaerospace.com

The detection methods proposed in this paper rely on having an estimate and a measurement of the surface temperature of a UAV wing subjected to icing. The advantage of having such an estimate is that it allows one to predict the nominal thermal dynamics of the wing in iced conditions. Thus, if an ice shedding event happens, the error between the predicted and the measured temperature will include information regarding the change in the temperature state of the wing, making it possible to develop ice shedding detection algorithms based on that change. In this study, the required temperature estimate is obtained through a Kalman filter (KF). This particular KF uses a first-order linear model that relates the heating panel power input to the temperature measured by the thermocouples in the wing. A standard KF implementation can output a KF innovation sequence, which is the difference between the sensor measurements and the KF predictions. By proper tuning, the KF innovation sequence can become the signal where ice shedding detections can be made. In this paper, two detection methods that utilize the KF innovation sequence are investigated: a method based on direct thresholding of the innovation sequence and a method based on detecting abrupt changes in the innovation sequence using continuous wavelet transform (CWT).

The use of KF residuals for change detection is not a new concept and is a rather widespread technique. In the aviation field, it has been used to detect structural changes in aerial vehicles, usually related to damage detection. For instance, in [17] Miller et al. develop an aircraft health monitoring system to make fault detections based on the change in the aerodynamic model-estimate-residuals. In [18] Sørensen et al. use KF residuals of the airspeed, lift and drag states in a generalized likelihood ratio test (GLRT) framework to identify icing conditions. A similar GLRT-based approach is used by Ding et al. in [19] to detect aircraft icing and by Hansen et al. in [20] to diagnose airspeed measurements in UAVs. When it comes to the CWT, similar use of the method can be found in [21] by Du et al., where it is used for peak detection in mass spectrometry data, in [22] by Nenadic and Burdick, where it is used for spike detection in neural-recordings, and by Zhang et al. in [23] where it is used for peak alignment in chromatography. Other applications and a more in-depth description of the CWT method can be found in [24] by Sadowsky.

The novelty of this study is twofold. Firstly, this study introduces the use of a linear first-order approximation of the distributed heat transfer dynamics in a composite UAV wing, which makes it possible to omit the use of the heat equations as it is done in [14] and [15]. Secondly, this study introduces the use of a KF innovation sequence and CWT-based pattern matching for ice shedding detection on the wings of a UAV.

The paper is structured as follows. Section II starts by presenting how the ice shedding detection problem is formulated from the standpoint of the available experimental data. It then presents the chosen ice shedding detection approaches, followed by a subsection on heat transfer modeling and system identification. Finally, in Section II the theory behind the developed detection algorithms is presented. Section III presents the final tuning of the developed detection algorithms and the detection results obtained using a validation data set. The limitation of the developed algorithms and the available experimental data are discussed in Section IV, and in Section V the concluding remarks regarding the results of the paper and future work are given.

II. Methods

The goal of this section is first to describe the experimental setup used to collect ice shedding data for this study and then explain the theory behind the methods developed for ice shedding detection on the wings of a UAV.

A. Data Acquisition and Experimental Setup

The data used in this study comes from icing wind tunnel tests performed at the Technical Research Center of Finland (VTT), using a test wing with an embedded electrothermal de-icing system. The icing wind tunnel at VTT is capable of reproducing realistic atmospheric icing conditions for low Reynolds numbers flights (Re = 8–9 $\times 10^5$) that are typical for small to medium-sized fixed-wing UAVs [25]. Furthermore, the icing wind tunnel at VTT is large enough to accommodate a full-scale wing section of a medium-sized UAV, equipped with a de-icing IPS, as shown in Fig. 2. The test wing section is a fiber-reinforced epoxy wing based on the RG-15 airfoil with a chord length of 0.30 m and a span of 0.65 m. The de-icing system built into the test wing consists of four electrothermal carbon-fiber heating elements, one heating wire that goes along the leading edge of the wing (the parting strip), and five thermocouples arranged as shown in Fig. 1 [9].

Data from the tests include temperature measurements from thermocouples, input power to each of the heating elements, and video recordings of the experiments, which were used to label ice shedding events and detect anomalies.

The built-in heating elements and temperature sensors are named according to their placement in the wing, with the following notation used throughout the paper: primary upper (PU), primary lower (PL), secondary upper (SU), secondary lower (SL) and parting strip (PS).

During the test campaign, several operating regimes of the de-icing IPS were tested. This included varying the amount of power supplied to each of the heating zones, varying the combination of the activated heating zones during the experiments, and variation of the ambient temperature. A subset of these experiments was chosen to develop the ice shedding detection methods in this study. The chosen operational regime utilized the PU, SU, and PS heating zones with power distribution as shown in Table 1. Additional information about the experiment setup, such as the range of ambient temperatures, the LWC and the wind speed, are provided in Table 1 as well.

Table 1   Operational regime of the de-icing system used to produce ice shedding data for this study.

Number of experiments	Temperature	Wind speed	LWC	Power PU	Power SU	Power PS
13	[-5°C , -10°C]	25 m/s	0.45 g/m^3	12 kW/m^2	6 kW/m^2	[20W, 50W]

The duration of each experiment is approximately 5 minutes, with slight variations due to operator reaction and varying ice shedding times. The experiments start as soon as the icing wind tunnel is turned on. Following the start of the experiment, the parting strip is set into the anti-icing mode, in which the PS continuously receives a fixed amount of power. The other heating zones are not yet activated at this point. The duration of the ice accretion period of the test is determined by how long it takes for enough ice to accumulate before the performance degradation becomes too big, at which point the IPS enters the de-icing mode. With this particular setup, it takes 4 minutes for the ice to build up to the desired level and initiate the de-icing mode. In de-icing mode, the heating zones are operated at a fixed power input until ice-shedding is observed visually. After ice-shedding has been observed, all heating zones are turned off, and the experiment is concluded. A representation of the amount of data collected from a single experiment is shown in Fig. 3, which includes power input and thermal measurements from the PU, SU, and PS zones. Moreover, an overview of the experiment phases can be seen in Fig. 4.
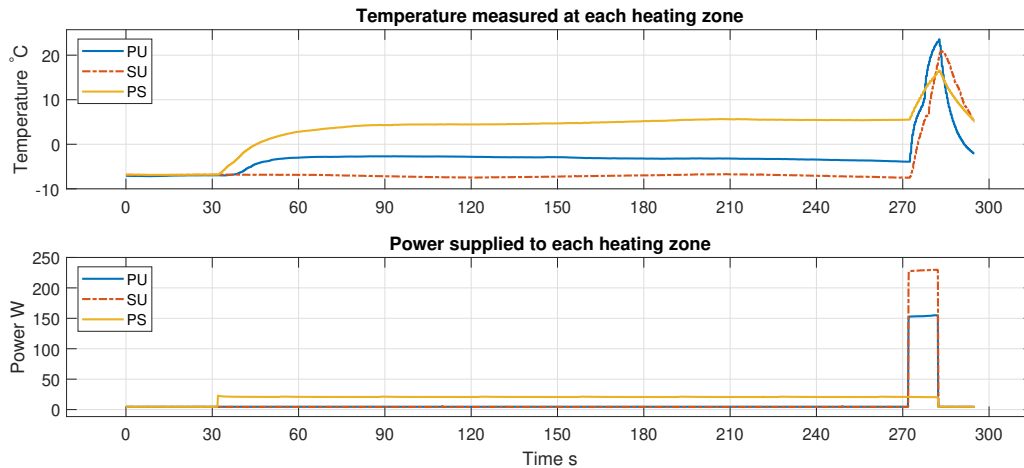

Fig. 3   Recorded temperature and power data for each of the heating zones PU, SU and PS, experiment 102.
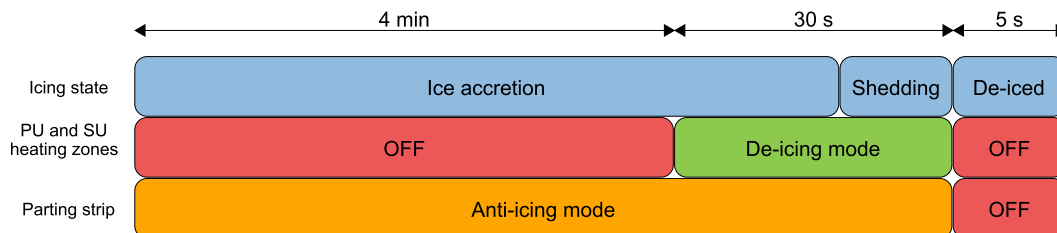

Fig. 4   An overview of the de-icing experiment phases.

Ice shedding events were labeled manually by going through video recordings of the experiments. The recordings were made using a high-speed camera and synchronized to Posix time, allowing for ice sheddings to be labeled with 0.1-second accuracy. Separate labels were made for ice shedding at the PU as SU zones. In three of the recorded experiments, the ice shedding happens simultaneously across both the PU and SU zones. In the rest of the experiments, there is a delay of a couple of seconds between the ice sheddings. Moreover, in some experiments, a partial ice shedding initiates the shedding. To simplify the labeling process, it was decided that in the case of partial shedding, the first shedding event would be labeled. This is deemed acceptable as, in all viewed cases, partial shedding always leads to complete shedding shortly afterward.

The temperature measurements and the power input data are available at a 10 Hz sampling rate. Furthermore, the temperature data is low-pass filtered with a cutoff frequency of 2.2 Hz, which removes high-frequency noise at the expense of adding an average delay of 0.4 seconds to the signal.

The methods used in this study are data-driven, which requires a split of the available experiment data into training, test, and validation sets to ensure that the final results are as unbiased as possible. The partition of the experiment data and its use can be seen in Table 2.

Table 2   Data set split

Split	Use-case	ID of included experiments
Training set	System identification, Section III.A	$\{68, 73, 104, 125\}$
Test set	KF and detection algorithm tuning, Sections III.B and III.C	$\{67, 71, 102, 124, 127\}$
Validation set	Assessment of the detection performance, Section III.D	$\{69, 103, 106, 126\}$

B. Ice Shedding Observability

The development of an ice shedding detection system depends mainly on the ability of the temperature sensors embedded in the test wing to measure changes caused by ice shedding. The available information about the manufacturing of the test wing and the temperature measurements indicate that the sensors' placement relative to the heating elements and the wing surface affects the ability of the sensors to sense ice shedding events. Moreover, the power level at which the heating zones are operated might also have an effect.

The sensitivity of the temperature sensors to ice shedding events used in this study can be seen in Fig. 5. It is clear, from the distinct secondary step-response measured by the PU sensor, that the PU sensor is highly sensitive to changes caused by ice shedding. The SU sensor, on the other hand, does not sense the ice shedding in the same manner. Here one can observe only a slight dip in the temperature right after the ice shedding. Lastly, the PS sensor does not exhibit any apparent change due to ice shedding. This is expected as the PS area is relatively narrow and is operated in the anti-icing mode throughout the experiment, which reduces the amount of accreted ice on the leading edge.
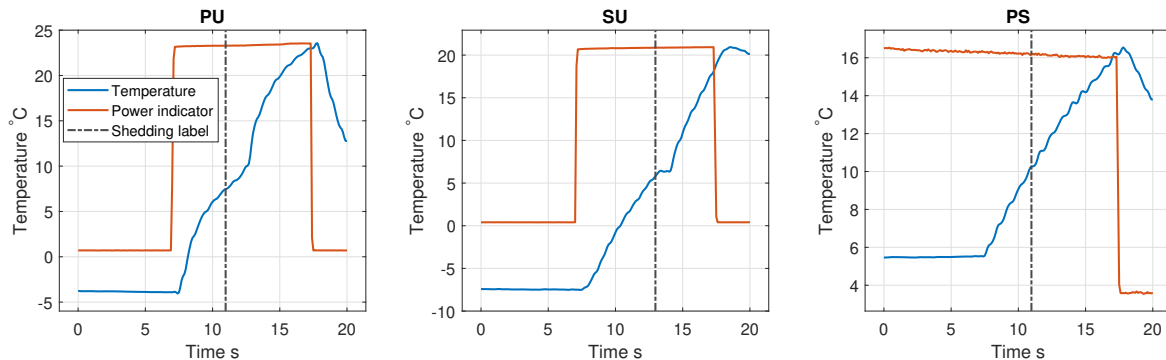

Fig. 5   Ice shedding response at each of the heating zones in experiment 102. The input power is scaled to the temperature measurements and is therefore only used as indicator of the de-icing mode activation.

The main cause for these variations is the inconsistent placement of the thermocouples relative to the heating elements and the wing's surface. This is also why two methods have been developed in this study, tailored to each type of the ice shedding-induced changes in PU and SU measurements.

C. Ice Shedding Detection Approach

The ice shedding detection approaches presented in this study use a KF innovation sequence as the signal where the detections are made. In signal processing, the innovation sequence is defined as the difference between the KF measurement prediction $\hat{y}_{k|k-1}$ and the actual measured temperature y_k at time step k, as shown in Eq. (1) [26]. In theory, during optimal operation, the innovation sequence has the properties of zero-mean white noise. This property is often used to tune the KF [27]; however, it can also be used to detect faulty behavior, which is exactly how it is used in this study.

$$\nu_k = y_k - \hat{y}_{k|k-1} \tag{1}$$

The problem of ice shedding detection in the case where the measured thermal dynamics change significantly due to ice shedding, such as in the PU heating zone, can be formulated as parameter change detection problem. In such a case, the detection problem can be implemented using a KF, where the innovation sequence is used to analyze the fitness of the underlying model to the measured dynamics. If the underlying model is accurate enough, a GLRT-based detection can be set up. This would allow for stochastic descriptions of the detection performance, providing probability for various detection types, such as false positive and false negative detections. In case the nominal model exhibits a clear persistent error, a simpler direct thresholding method can be applied, where a significant enough deviation from zero in the innovation would indicate a poor fit of the model to the measured dynamics.

The problem of ice shedding detection in the case where the measured thermal dynamics change only slightly but nonetheless abruptly, such as in the SU heating zone, can be formulated as intermittent noise detection problem. With the KF framework, one possibility is to use the KF innovation sequence to highlight the intermittent noise caused by ice shedding. Assuming that the intermittent noise caused by ice sheddings is consistent across the experiments, one can develop a pattern matching algorithm to detect it. In this study, the CWT is used as a pattern matching method to detect the ice shedding events.

D. Heat Transfer Modeling

The KF innovation sequence is at the core of the developed detection algorithms. To set up a KF and produce the desired innovation sequence, a heat transfer model that relates the power input of the heating elements to the temperature measurements, as well as measured ambient conditions, are necessary.

The particular approach chosen in this study to model the heat transfer in the UAV wings is based on system identification of a delayed first-order linear model. In reality, heat transfer is a more complex process that is more accurately described by distributed heat convection and conduction dynamics. However, due to several factors such as available information about the UAV wing, the amount of available experiment data, the domain knowledge of the researchers, and the desire to make an easily implementable detection algorithm, it was first chosen to go with a simple first-order model of the following form:

$$\dot{x}(t) = a(T_{amb} - x(t)) + bu_{(*)}(t)$$
$$y(t) = x(t) \quad , \tag{2}$$

where $u_{(*)}(t)$ is the input from the heating zone $(*) \in [PU, SU, PS]$, $x(t)$ is the modeled temperature at that heating zone, $y(t)$ is the model output, T_{amb} is the ambient temperature and (a, b) are model parameters. Since heat transfer is a distributed process, the simple model in Eq. (2) is not able to describe the process satisfactorily. To improve the model's fitness to the observed heat transfer dynamics, two modifications are made: a time delay is introduced on the input side, and an additional input source is added to account for the heat from the second nearest heating zone. The final heat transfer model used in this study has the following form:

$$\dot{x}(t) = a(T_{amb} - x(t)) + b_1 u_1(t - \tau_1) + b_2 u_2(t - \tau_2)$$
$$y(t) = x(t) \quad , \tag{3}$$

where τ is the time delay in seconds, and the subscripts $(1, 2) \in [PU, SU, PS]$ refer to the input power sources.

In Eq. (3), $[a, b_1, b_2, \tau_1, \tau_2]$ are the unknown model parameters which can be identified through system identification. During the system identification process, it is important to be aware that model parameters change after the ice shedding occurs. This is, in fact, the key assumption for the developed ice shedding detection methods. For this reason, only the data recorded prior to the observed ice shedding is used to fit the nominal model parameters, as highlighted in Fig. 6. The highlighted area goes slightly beyond the ice shedding labels as it takes time for the sensors to pick up ice shedding-related changes.
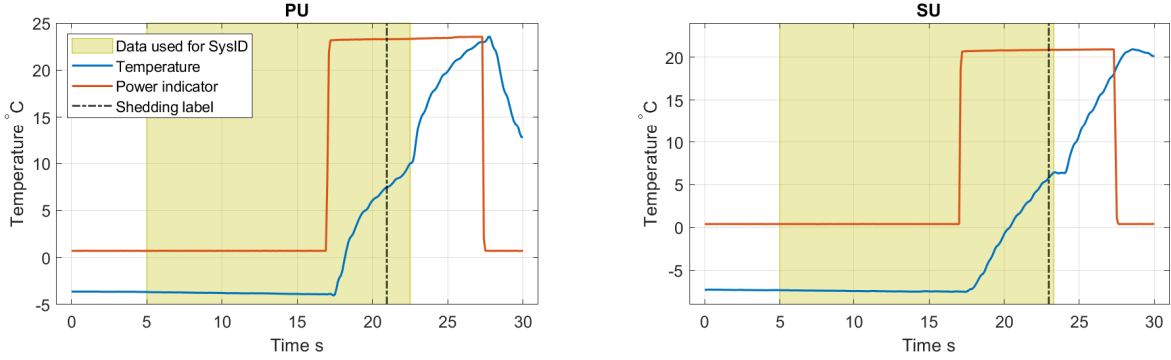
6

Fig. 6 Section of the experiment data used to fit the heat transfer model in iced conditions.

The particular offline system identification method used in this study is based on non-linear gradient descent with root mean square error (RMSE) minimization as the optimization metric. In practice, it is implemented by using the MATLAB solver *fmincon* [28]. This solver works by running the desired model, in this case given by Eq. (3), in an open-loop simulation and comparing the simulation output to the temperature measurements. The RMSE of the compared signals is then used to update the model parameters. This loop of simulation, comparison, and parameter update is performed several times until the computed RMSE stops changing or reaches a specified lower threshold. The optimal time delays (τ_1, τ_2) are found by testing a range of values and selecting the ones that give the lowest RMSE. The nominal models for PU and SU zones are found offline before the ice shedding detection algorithms are activated and tested.

E. Kalman Filtering
The KF is a well-known state estimator that fuses two sources of information to produce an optimal state estimate [29]. The two information sources are the system dynamics provided by the process model and the available state measurements. An adaptive gain in the filter varies the weighting ratio of the two information sources used to predict the future system state. If the state measurements are accurate, the adaptive gain prioritizes the measurements. If the measurement error is substantial, the system dynamics and the measurements are weighted more equally by the adaptive gain. In case no measurements are available, the KF works as an open-loop model simulation.

Tuning of the KF is an important topic that, for complex models, can be elaborate. However, since the underlying model, in this case, is a first-order model and the noise covariance matrices are scalar, the KF can be tuned by simply adjusting the ratio between the process- and measurement noise covariances, R_1, R_2 [30]. Note that while R_2 is given by sensor characteristics, R_1 should be chosen small in order to create a residual with a significant steady-state error when the nominal model is not matching the measured dynamics, in this case, after ice shedding.

F. Continuous Wavelet Transform
One of the ice shedding detection algorithms presented in this study is based on pattern matching in the KF innovation sequence. The chosen pattern matching method is a thresholded CWT, which results in a binary signal that is active when a potential detection is made.

CWT is a signal analysis method that is suitable for pattern matching in non-stationary signals [22, 31]. The method is based on spectral convolution of the signal of interest, in this case ν from Eq. (1), and a wavelet function $\psi_{c,d}(t)$ given in Eq. (4), at different scales and time intervals defined by c and d.

$$\psi_{c,d}(t) = \frac{1}{\sqrt{|c|}} \psi\left(\frac{t-d}{c}\right) \tag{4}$$

Mathematically the spectral convolution is formulated in the following way:

$$C(\psi, c, d) = \int_{-\infty}^{\infty} \nu(t)\psi_{c,d}(t)dt \quad . \tag{5}$$

The integral in Eq. (5) calculates CWT-coefficients for every wavelet scale c and time-shift d. The CWT-coefficients represent the similarity of the wavelet $\psi_{c,d}(t)$ to the innovation sequence $\nu(t)$ at location $t = d/c$. The result of a CWT is a 2D grid of CWT-coefficients, $C_{i,j}$, which are typically visualized through a scalogram with the scale-dependent frequency on the y-axis and time on the x-axis. The tuning of the CWT method is based on the choice of the wavelet function $\psi(t)$ and the chosen range of the wavelet parameters (c, d) to be iterated over. In this study, the CWT-based detection algorithm was implementation with MATLAB's Wavelet Toolbox [32] using the Morse wavelet [33]. The selection of the wavelet was made by visually matching the shape of the typical dips caused by ice shedding to the available wavelets in the MATLAB's CWT function, as well as testing to see which wavelet type and tuning produced the highest activation at the points of ice shedding in the innovation sequence.

On a practical note, in the MATLAB implementation of the CWT function, one does not tune the (c, d) parameters but rather the parameter γ, which controls the symmetry of the wavelet in time and parameter P^2 which is proportional to the wavelet duration in time [34].

G. The Detection Algorithms

The final outcome of a detection algorithm has to be a detection. To this end, the algorithms developed in this study use a binary signal $L[k]$ to carry the detection state, where zero indicates no detection, and one indicates detection.

In the case of direct thresholding, a decision is made at each time step k by thresholding the KF innovation ν_k using a specified threshold value α as shown in Eq. (6):

$$L_k = \begin{cases} 0, & \text{if } \nu_k < \alpha \\ 1, & \text{otherwise} \end{cases} \quad . \tag{6}$$

To remove the effect of signal oscillation on the threshold-based detections, the switching function in Eq. (6) is implemented with hysteresis. Thus, if the innovation value ν_k crosses the threshold α and triggers a detection, it would have to fall below the hysteresis region, which can be about 80% of the α value, before the detection state is reverted to 0.

In the CWT-based detection algorithm, the detection decision is more complicated. The CWT is performed on a sliding window of the innovation sequence $\nu[k - n : k]$ of size n, resulting in a 2D coefficient matrix $C_{i,j}$ where i spans the frequency domain and j is the length of n and spans the time domain. The values in $C_{i,j}$ are complex; therefore, the magnitude of each coefficient has to be computed before they can be used further. To obtain a one-dimensional output signal, the CWT values in $|C_{i,j}|$ are collapsed along the frequency dimension i using averaging, resulting in a real-number sequence with a length of the sliding window. Finally, the maximum value in the averaged coefficient sequence is found and thresholded by the specified thresholding value α_{cwt}.

$$C_{1D}[j] = \frac{1}{N} \sum_{i=1}^{N} |C_{i,j}| \quad , \quad i \in [1, .., N] \,, \, j \in [1, .., n] \tag{7}$$

$$L_k = \begin{cases} 0, & \text{if } \max(C_{1D}) < \alpha_{cwt} \\ 1, & \text{otherwise} \end{cases} \tag{8}$$

Similar to the switching function for the direct thresholding method, the function in Eq. (8) is implemented with hysteresis. Moreover, due to edge effects associated with wavelet transforms [35], only the inner 80% of the 1D coefficient sequence are used in the final detection,

$$\max(C_{1D}[0.1n : 0.9n]) < \alpha_{cwt} \quad . \tag{9}$$

Both threshold values α and α_{cwt} were found manually by tuning the detection algorithms on the test set.

III. Results

This section presents system identification, KF and CWT tuning and the ice shedding detection results.

A. System Identification

The results of system identification are given in Table 3. The model structure used to fit the data is given in Eq. (3). The model has five parameters that need to be identified: $[a, b_1, b_2, \tau_1, \tau_2]$. The data used for system identification

includes a section of the recorded experiments that starts about 10 seconds before the activation of the de-icing mode and continuous until the observed ice shedding event, thus providing a heat transfer model in iced conditions, see Fig. 6 for a visual explanation. Parameters of fitted models that describe the heat transfer measured at the PU and SU zones are presented in Table 3. No model was identified for the PS zone as no change due to ice shedding was observed there.

Table 3   Identified model parameters.

Parameters Model	a	b_1	b_2	τ_1	τ_2
PU	0.5018	0.0247	0.0048	0.6 s	4.9 s
SU	0.1209	0	0.0123	—	1.0 s

The results in Table 3 are reasonable as the relative placement of the thermocouples between the heating elements and the wing's surface is not consistent at each heating zone. This leads to the variable ability of the sensors to pick up changes due to ice shedding events discussed in Section II.B. Furthermore, this inconsistency leads to varying proximity of the sensors to the surrounding heating elements, thus affecting the sensors' ability to register heat from those sources. For instance, as seen in Table 3, the model for the SU sensor only includes one input $b_2 u_2(t - \tau_2)$, while $b_1 = 0$.

B. Kalman Filter Tuning

The goal of KF tuning is to ensure that the KF performs well during nominal conditions, i.e., conditions before ice shedding, and produces significant non-zero innovations after ice shedding. Thus, making it possible to develop a detection based on the amplitude of the innovation sequence. In Fig. 7 three tuning variants have been tested. The R_1 matrix, in this case a scalar, represents the process noise covariance, i.e., the model uncertainty. The R_2, also a scalar in this case, describes the measurement noise covariance, which largely depends on the sensor characteristics.

As seen in Fig. 7, the filter exhibits desired characteristic with the $(R_1, R_2) = (10^{-3}, 10^{-1})$ tuning. With this tuning the filter performs adequately in the nominal condition by producing near-zero innovations. Moreover, after ice shedding a clear amplitude increase and a persistent error is observed in the innovation sequence. This is exactly the desired behavior of the KF innovation sequence in iced and ice-free conditions. The tuning parameters $(R_1, R_2) = (10^{-3}, 10^{-1})$ are therefore selected to produce the signal for the ice shedding detection algorithms in this study.
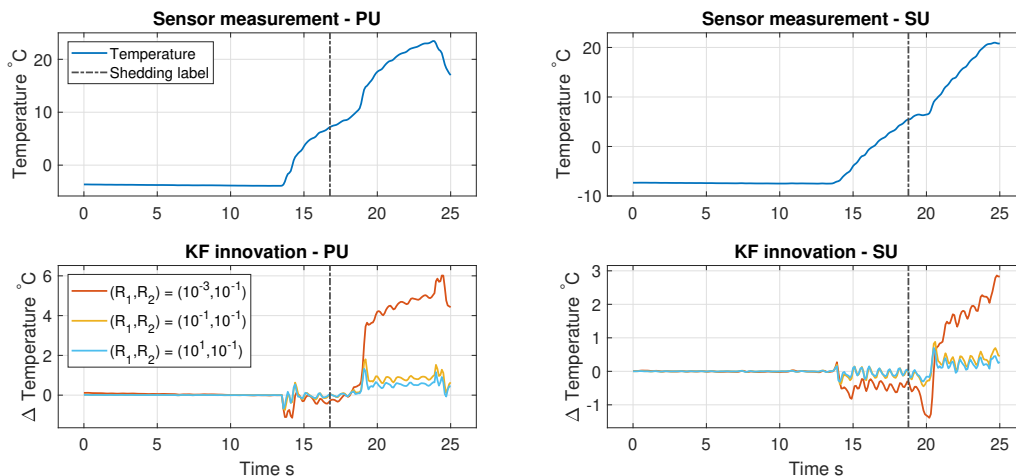

Fig. 7   KF innovation sequences obtained with three different KF tunings. Temperature measurements and ice shedding labels are shown in the upper row, the associated KF innovations in the lower row.

The same KF tuning is used for both the PU and SU zones. However, when comparing the identified models for the PU and SU zones, one can see that the PU model is more precise with respect to the actual heat transfer dynamics. This is evident from the negative bias of the SU innovation sequence, which becomes more clear when the KF is tuned such that it weighs the model prediction more than the measurement correction, in practice achieved by setting R_1/R_2

sufficiently small. Nonetheless, the negative bias in the SU innovation does not cause any significant problems for the threshold-based detection method, and no further tuning is performed for the SU zone specifically.

C. Continuous Wavelet Transform Tuning

The goal of the CWT is to output a signal where the ice shedding events produce clear and detectable activations. Manually testing the CWT on the test set showed that among the available wavelets in the MATLAB's implementation, the Morse wavelet with parameters $(\gamma, P^2) = (2.9, 3.0)$, discussed in Section II.F, gave the highest activation of the ice shedding related dips present in the SU innovation sequence.

Unlike the CWT application in the SU zone, in the PU zone it is not used for pattern matching. Instead, the CWT output is used to detect the abrupt increase in the amplitude of the PU innovation sequence caused by ice shedding. As such, no additional tuning had to be done, and the same wavelet and wavelet parameters were used for both zones. The result of applying CWT to the PU and SU innovation sequences from experiment 102 is shown in Figure 8.

(a) PU data from experiment 102
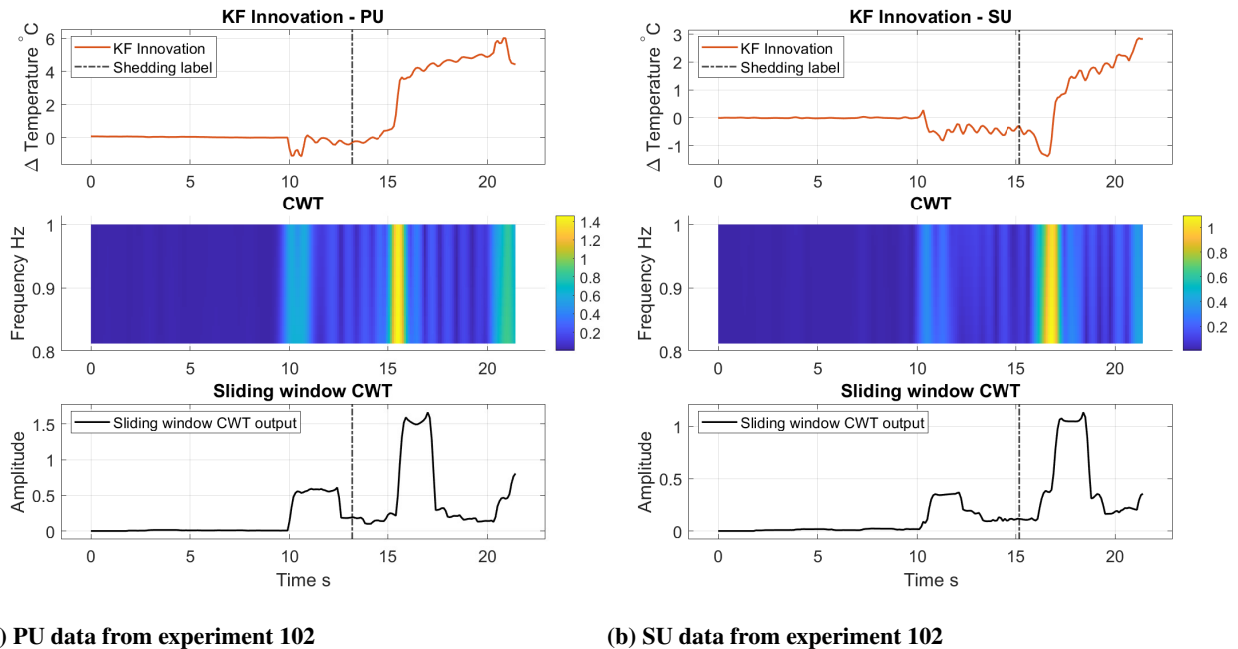
(b) SU data from experiment 102

Fig. 8   CWT and sliding window CWT applied to the PU and SU KF innovation sequences. Results obtained using the Morse wavelet with parameters $(\gamma, P^2) = (2.9, 3.0)$ and a two seconds long sliding window.

The outputs of the sliding window CWT algorithms in Figs. 8a and 8b are the maximum CWT-coefficient values extracted from each consecutive sliding window. The calculation of the sliding window CWT is given in Eqs. (7)–(9). The sliding window, in this case, is two seconds long. The size of the sliding window influences how long each activation is sustained. Thus, the sliding window should be short if the goal is to detect each dip in the innovation sequence separately. A typical ice shedding-related dip in the SU innovation sequence is about one to two seconds long. Thus, the sliding window should span at least two seconds in this case.

Given the sliding window CWT output, a detection method can be developed. However, absent any additional logic, a detection threshold would have to be set quite high such that it does not get overcome by the first peak in the signal, which is related to the initialization of the de-icing system, as seen at 10-second mark in Figs. 8a and 8b. One straightforward solution to this is to delay the initialization of the CWT-based detection algorithm by three seconds, such that the initial peak is not registered. This allows setting a lower detection threshold, which increases the method's sensitivity and gives shorter detection times. Based on the fact that ice shedding events are measured with a delay and the fact that in the training- and test sets the average ice shedding times for the PU and SU zones are 6.5 and 7.7 seconds, respectively, a three-second delayed initialization is deemed a reasonable solution to the initial peak problem. Furthermore, to simplify the algorithm and make it usable as an input to a de-icing IPS, the first CWT-based detection is sustained until the reset of the algorithm. The two CWT-based algorithms presented here are referred to as the raw and the improved CWT-based detection algorithms, both of which are tested and assessed in this study.

D. Detection Results

Both the direct KF thresholding method and the sliding window CWT-based methods have been able to detect ice shedding in the four experiments of the validation set. The detection times for PU and SU zones can be seen in Fig. 9. The detection threshold values, tuned based on the training- and test set data, are provided in Table 4. A visualization of the ice shedding detections in the PU and SU temperature measurements can be seen in Figs. 10a and 10b. Figures showing the results for the rest of the validation set can be found in the Appendix. As discussed in the section regarding the ice shedding detection approach, Section II.C, there is a difference in the sensitivity of the temperature measurements to the ice shedding events in the PU and SU zones. The ice shedding significantly changes the PU zone measurements, making it easy to detect ice shedding using the simpler direct thresholding method. In the SU zone, the ice shedding is not as noticeable, thus increasing the relevance of the CWT-based methods.
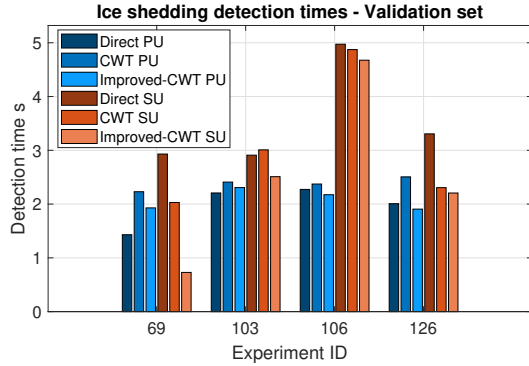

Fig. 9   Validation set detection times.

Table 4   Detection thresholds for the direct thresholding and CWT-based algorithms.

Zone	Threshold type	Value
PU	KF innovation threshold	$\alpha_{\mathrm{PU}} = 1.0$
	CWT threshold	$\alpha_{\mathrm{PU,cwt}} = 0.95$
	Improved-CWT threshold	$\alpha_{\mathrm{PU,imp\text{-}cwt}} = 0.30$
SU	KF innovation threshold	$\alpha_{\mathrm{SU}} = 1.0$
	CWT threshold	$\alpha_{\mathrm{SU,cwt}} = 0.45$
	Improved-CWT threshold	$\alpha_{\mathrm{SU,imp\text{-}cwt}} = 0.35$

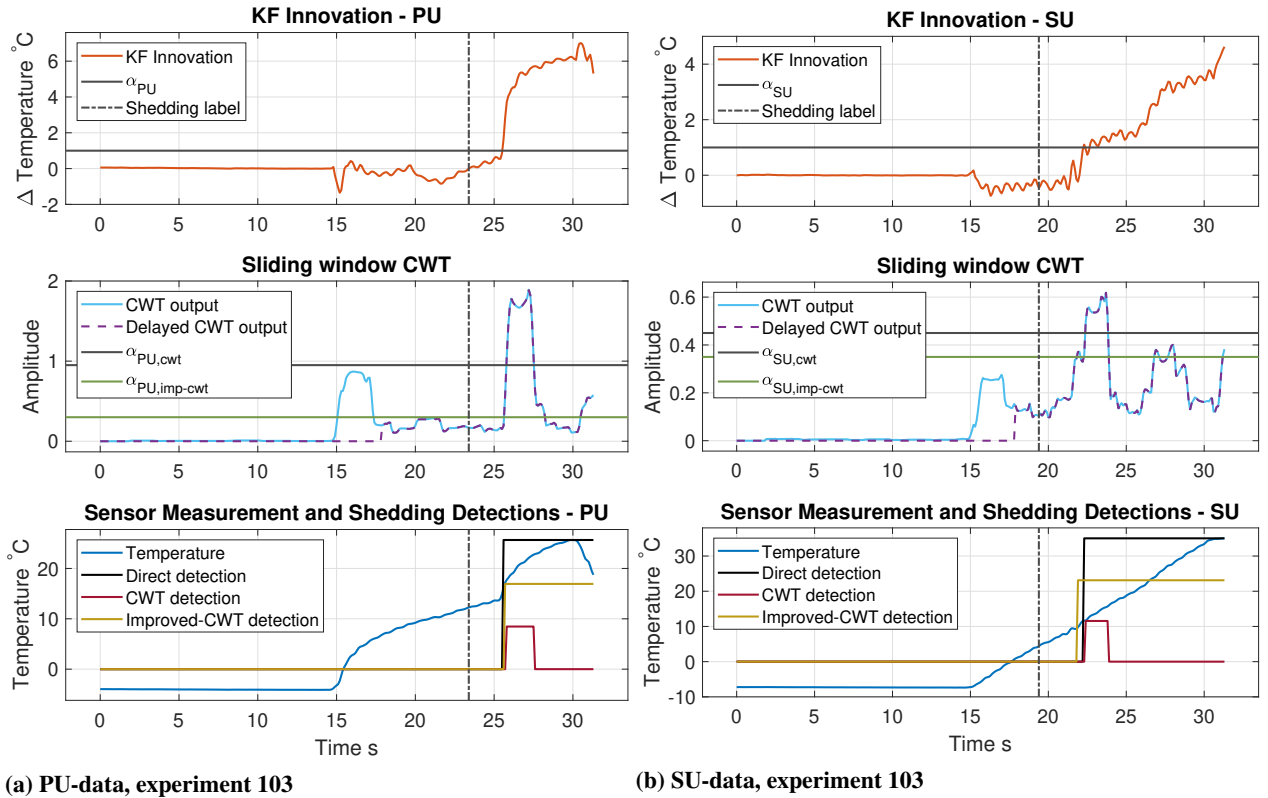(a) PU-data, experiment 103

(b) SU-data, experiment 103

Fig. 10   Ice shedding detections in PU (a) and SU (b) zones made using the developed detection algorithms — experiment 103, validation set.

11

Unlike the direct thresholding method and the improved CWT-based method, the raw CWT-based method produces several false positive- and false negative detections. These are falsely made detections and missed detections, respectively. What these type of detections look like in the context of ice shedding detection in a KF innovation sequence is shown in Fig. 11a and Fig. 11b. In Fig. 11a none of the CWT activations breach the $\alpha_{\text{SU,cwt}}$ threshold and trigger a raw CWT-based ice shedding detection, while in Fig. 11b a dip in the innovation sequence at about 33 seconds, not associated with an ice shedding event, leads to a CWT-based detection. One notable characteristic of the false positive detections made by the raw CWT-based method is that all of them happen after the actual ice shedding, meaning there are no detections that would indicate ice shedding before it has happened, except the peak due to initialization of de-icing which is deliberately removed by delaying the sliding window CWT in the improved method. This characteristic is also the reason it has been possible to lower the detection threshold for the improved CWT-based method without producing any false positive detections. However, the fact that the raw CWT-based method produces several false positive detections after the ice shedding indicates that this method is more sensitive to noise in the innovation sequence compared to the direct thresholding method.
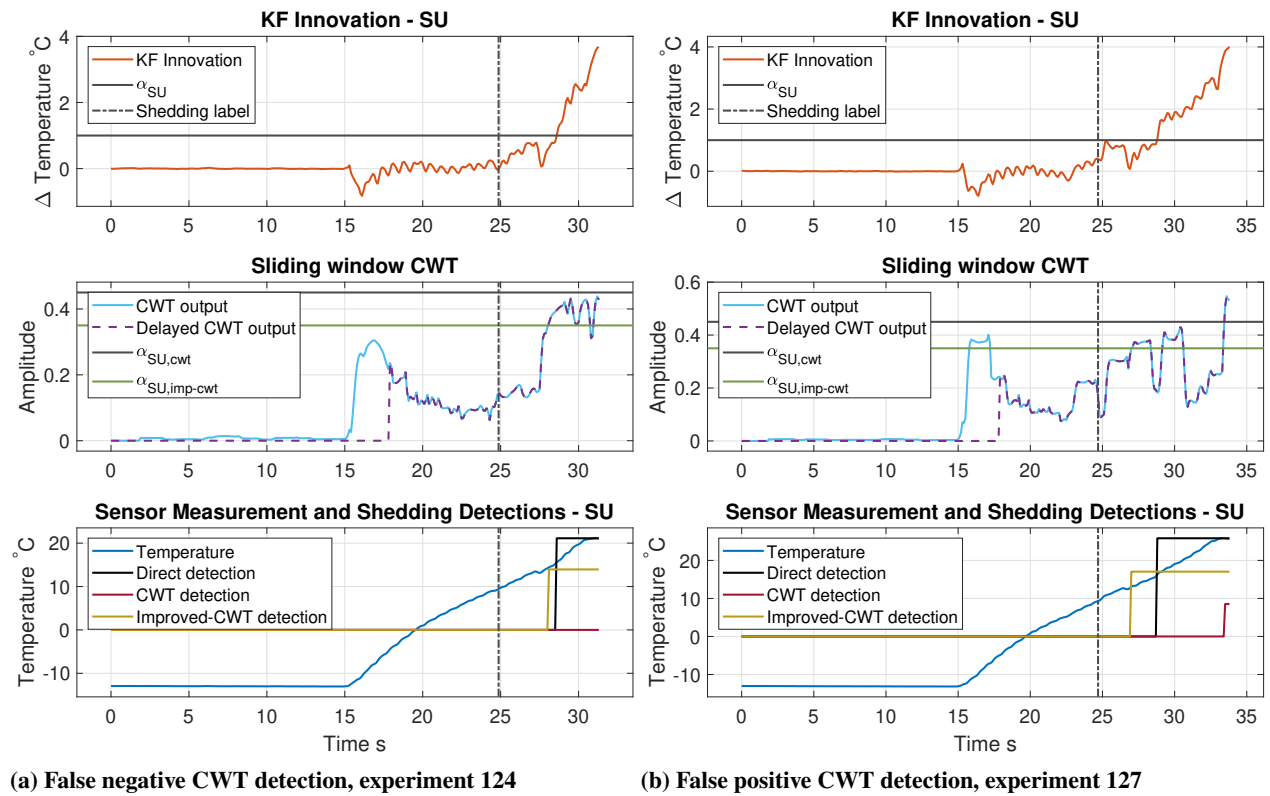

(a) False negative CWT detection, experiment 124   (b) False positive CWT detection, experiment 127

Fig. 11   Examples of false positive- and false negative detections made by the raw CWT-based algorithm.

The total number and the type of detections made by the raw CWT-based method in the train, test, and validation sets are provided in Table 5.

Table 5   Detections made by the raw sliding window CWT method, split by the data set and zone.

Detection type	Number of detections - PU		Number of detections - SU	
	Train & Test set	Validation set	Train & Test set	Validation set
False positive	0	1	3	5
False negative	0	0	2	0
True positive	9	4	7	4

Performance of the raw CWT-based method is quantified by precision, recall and the F-measure, defined in Eq. (10), the performance numbers are provided in Table 6.

$$\text{F-measure} := \frac{2 \times \text{precision} \times \text{recall}}{\text{precision} + \text{recall}} \tag{10}$$

Table 6   Analysis of the raw CWT-based detection method.

		Precision		Recall		F-measure	
		Train & Test	Validation	Train & Test	Validation	Train & Test	Validation
Zone	PU	1.00	0.80	1.00	1.00	1.00	0.89
	SU	0.70	0.44	0.78	1.00	0.74	0.61

The direct thresholding method and the improved CWT-based method both detect all of the ice shedding events without any false negative detections, resulting in the perfect precision and recall score of 1.0. The average detection times and the F-measure scores for all of the tested methods are given in Table 7. To make the calculation of the average detection times fair between the detection methods, the SU data in experiments 124 and 127 were excluded. This is done as the raw CWT-based algorithm does not produce true positive detections in the SU zone in these experiments.

Table 7   Performance analysis of the ice shedding detection algorithms, σ indicates the standard deviation.

		F-measure		Average detection time	
Zone	Method	Train & Test	Validation	Train & Test	Validation
PU	Direct	1.00	1.00	2.02 s ($\sigma = 0.45$ s)	1.98 s ($\sigma = 0.38$ s)
	CWT	1.00	0.89	2.31 s ($\sigma = 0.44$ s)	2.38 s ($\sigma = 0.11$ s)
	Improved-CWT	1.00	1.00	2.07 s ($\sigma = 0.46$ s)	2.08 s ($\sigma = 0.19$ s)
SU	Direct	1.00	1.00	2.75 s ($\sigma = 0.84$ s)	3.53 s ($\sigma = 0.98$ s)
	CWT	0.74	0.61	2.05 s ($\sigma = 0.87$ s)	3.05 s ($\sigma = 1.28$ s)
	Improved-CWT	1.00	1.00	1.70 s ($\sigma = 1.08$ s)	2.53 s ($\sigma = 1.63$ s)

In general, the detection results can be split and compared in the following three sub-groups: (i) performance across the heating zones PU and SU, (ii) difference between the raw and the improved CWT-based methods, and (iii) relative performance of the direct thresholding method and the improved CWT-based method in PU and SU zones.

(i) Analysis of the detection results in the validation set shows that it is easier to make detections in the PU zone. All three algorithms perform with shorter detection times and smaller standard deviations. This difference in performance between the zones can be mainly attributed to the ability of the sensors in each of the zones to pick up changes caused by ice shedding. (ii) When it comes to the CWT-based methods, it is clear that the improved version performs significantly better in both PU and SU zones, making faster detections and achieving a perfect F-measure score of 1.0. (iii) Comparing the direct thresholding method and the improved CWT-based method in the PU zone, one can see that both methods perform well with similar results. This can be explained by the fact that ice sheddings produce an abrupt and clear change in the PU innovation sequence, which is easy to detect using both methods. When it comes to the comparison of the detection results in the SU zone, one can see that while in terms of the F-measure, the performance is the same, the improved CWT-based method performs substantially faster with one second or about 30% shorter detection times, in both training, test and validation sets. However, the consistency of the improved CWT-based method is reduced, resulting in a larger standard deviation of the detection times. This can be attributed to the higher sensitivity of the improved method, which can easier get triggered by partial ice shedding events and therefore produce shorter detection times, such as in the case of experiment 69, see Fig. 9 for the detection times. Furthermore, although the improved CWT-based method doesn't make any false detections, the raw version of the algorithm at its base does. Finally, due to the small size of the validation set, it is difficult to assess whether the shorter detection times of the CWT-based method are worth the higher risk of false positive detections.

IV. Discussion

Several working solutions for real-time electro-thermal-based ice shedding detection on the surface of a UAV wing have been presented in this paper. However, the limitations of the proposed methods have not yet been discussed.

There are three main limitations to the methods that have been presented. The first limitation is that the models developed in Section II.D and identified in Section III.A are relevant only for one heating regime of the de-icing system. As shown in Table 1 the experiments in this study were conducted using the $[12\text{kW/m}^2, 6\text{kW/m}^2, 20\text{-}50\text{W}]$ regime of the de-icing system. Performing system identification on experiments with heating regimes $[12\text{kW/m}^2, 12\text{kW/m}^2, 50\text{W}]$ and $[8\text{kW/m}^2, 4\text{kW/m}^2, 8\text{W}]$, yielded substantially different models. As a result, a separate model has to be identified for each heating regime of the de-icing system. Alternatively, the model parameters have to be redefined as functions of the supplied power, which increases the model complexity. In general, both alternatives are achievable. The difference lies in that for the case where a set of models is used, a more complex implementation of the algorithm is required, while for the case with a more complex model, a substantially larger dataset is needed to identify the model reliably. Ideally, one would like to identify a linear first-order model that would work for all heating regimes. However, this is complicated by the fact that the heat transfer delay τ was observed to be a function of the heat power u, which varies depending on the heating regime of the de-icing system. Additionally, the modeling is complicated by the fact that the underlying system is more accurately described as a distributed process driven by heat conduction and convection dynamics. Nevertheless, considering the discussed complexities and the amount of available data, the modeling choices presented in Section II.D are deemed reasonable.

The second limitation concerning the methods developed in this study is that they have not been tested under continuously repeated icing and de-icing conditions. Such testing would have made it possible to assess the post-shedding performance and develop reset functionality for the developed detection algorithms. Furthermore, the experimental data were collected in static lab conditions, introducing the possibility of experiment-related bias in the results.

The third noteworthy limitation can be attributed to the size of the available data set. This study is based on data from 13 experiments, four of which are used to validate the developed algorithms. Smaller data sets make it more challenging to validate performance results, especially when two or more methods are compared. For this reason, it isn't easy to give a definitive answer on whether the direct innovation thresholding method or the improved CWT-based method is the best choice for ice shedding detection in the SU zone. That said, given the results of this study, it is possible to state that fast and precise real-time electro-thermal-based ice shedding detection is possible in both the PU and SU zones.

V. Conclusion

This study has presented and analyzed two different approaches to the electrothermal ice shedding detection problem: a parameter change detection approach implemented as direct thresholding of a temperature-estimating KF innovation sequence and a pattern matching approach implemented using the CWT of the innovation sequence. Algorithms developed using both approaches have been tuned and validated using icing wind tunnel experiments. The concluding results of this study show that one can successfully use thermal measurements to detect ice shedding on a UAV wing equipped with an electrothermal de-icing system. More specifically, the results indicate that given temperature measurements, where ice shedding is easily observable, the developed direct thresholding algorithm can consistently provide fast detections with a perfect F-measure of 1.0. On the other hand, in some cases, the analysis shows that the developed improved CWT-based algorithm might be better than the direct thresholding approach. This stems from the fact that in cases where ice shedding leads to minor changes in the innovation sequence, both approaches yield the same F-measure of 1.0, but the improved CWT algorithm makes detections up to one second or 30% faster. The improved CWT-based algorithm is, however, more likely to be affected by noise in the innovation sequence, and without a larger data set, it is difficult to assess whether the shorter detection times are worth the increased risk of false detections.

The purpose of the developed ice shedding detection algorithms is to optimize de-icing IPSs by providing an indicator for when to stop the heating process, such that the least possible amount of energy is wasted. The final validation set results show that it is possible to achieve an average ice shedding detection time of 1.98 seconds in the PU zone and 2.53 seconds in the SU zone. Thus, the results indicate that using these detection algorithms, one can substantially reduce the amount of required heating energy when compared to the base case where the IPS operates irrespective of the ice shedding status. The difference in the average detection times between the zones is explained by the ability of the respective temperature sensors to measure change caused by the ice shedding events, which differs mainly due to the relative placement of the sensors between the heating zones and the wing's surface.

Regarding the importance of the temperature sensor placement in the UAV wing; this study clearly shows that placement of the sensors can have a significant impact on the ability of the sensors to pick up changes caused by ice

shedding. Therefore, placing sensors such that similar ice shedding observability is ensured across all sensors, can make testing and validation of the developed detection algorithms easier.

When it comes to future work, based on the limitations presented in the discussion section Section IV, the following improvements can be made:
- Extend the fitted model to a bank of models where each model is fitted to each specific heating regime of the de-icing system.
- Collect a more extensive data set, including recordings of continuous icing/de-icing cycles.
- Test the integrated use of an electrothermal ice detection algorithm, such as the one described in [18], together with the ice shedding detection algorithms developed in this paper.

Additionally, given a setup with required sensors, a possible way forward is to see whether the developed ice shedding detection algorithms can be used to optimize rotor IPSs in UAVs, which is also currently an active field of research [36].

In the broader context, the goal of ice shedding detection algorithms presented in this paper is to make the UAVs safer and increase their utilization potential in all weather conditions, including icing. Moreover, as discussed in the introduction section, improving the UAV technology is highly relevant now as UAVs have recently shown to be extremely valuable for critical missions.
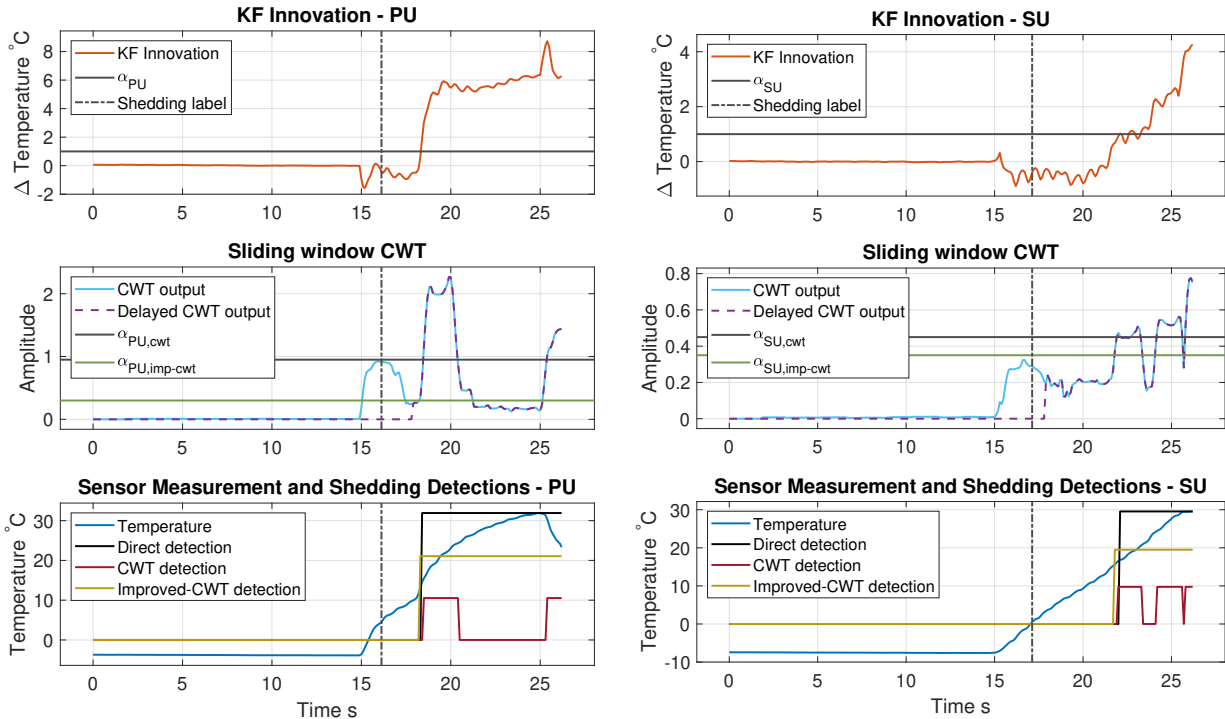
Appendix
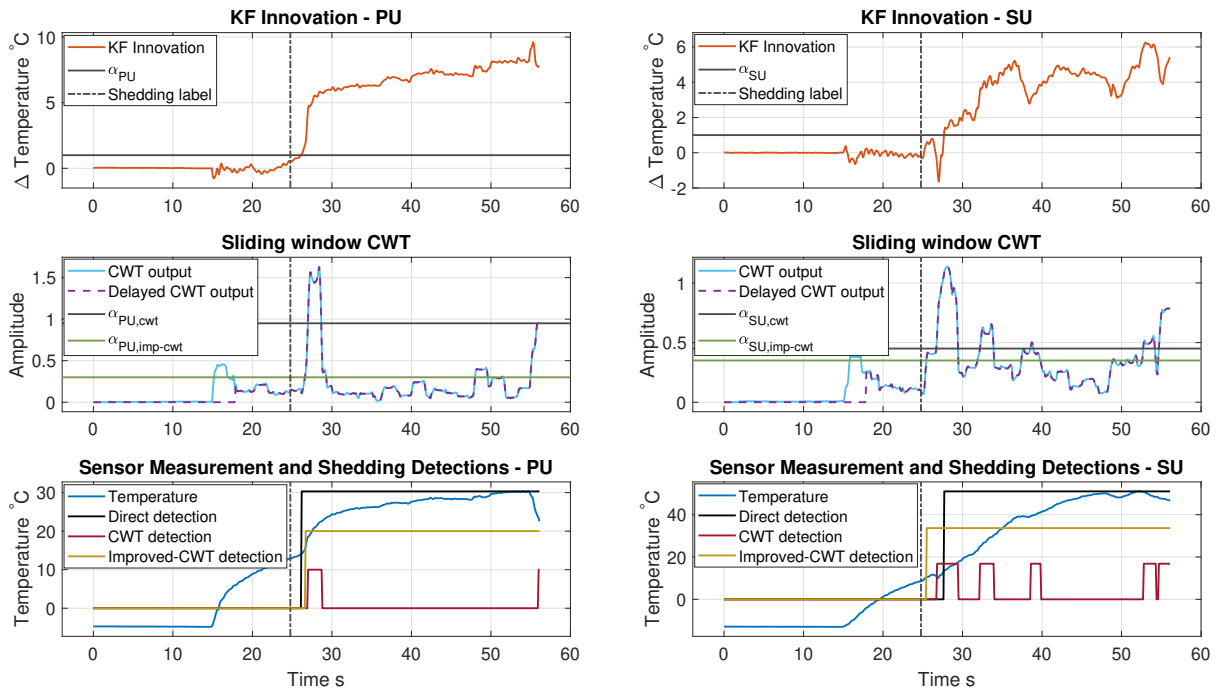
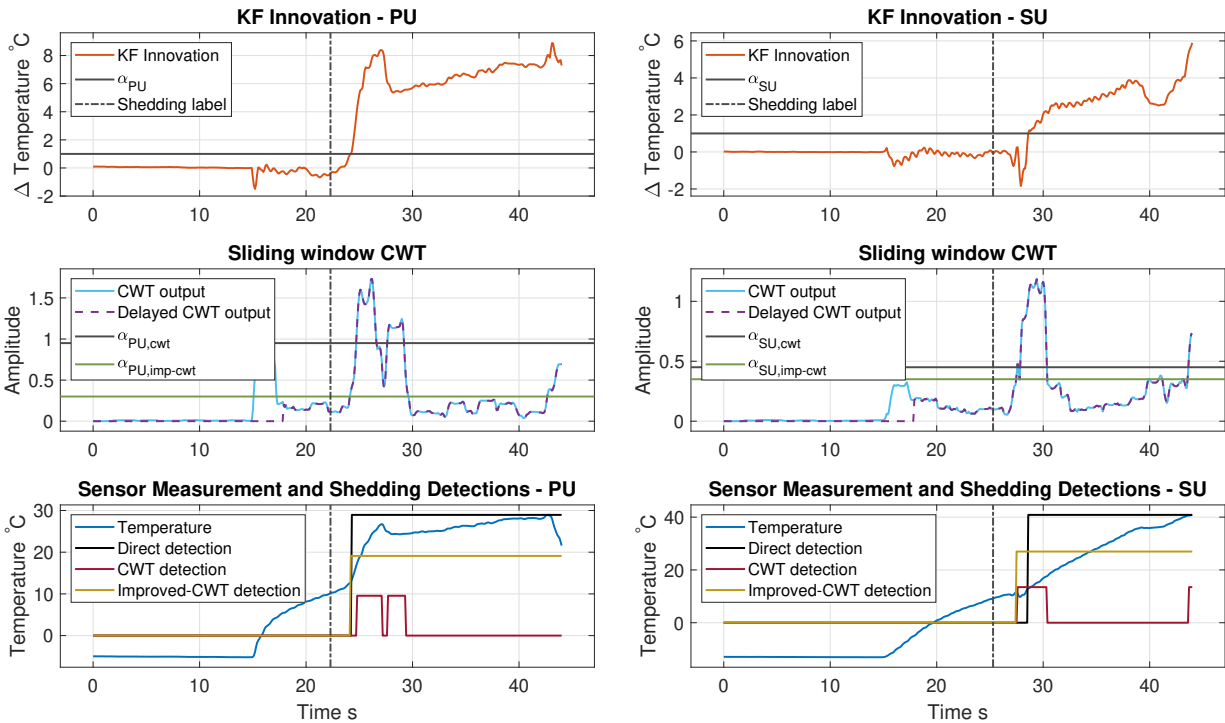(a) PU-data, experiment 69   (b) SU-data, experiment 69

Fig. 12   Ice shedding detections in PU (a) and SU (b) zones — experiment 69, validation set.

(a) PU-data, experiment 106

(b) SU-data, experiment 106

Fig. 13 Ice shedding detections in PU (a) and SU (b) zones — experiment 106, validation set.

(a) PU-data, experiment 126

(b) SU-data, experiment 126

Fig. 14 Ice shedding detections in PU (a) and SU (b) zones — experiment 126, validation set.

Acknowledgments

References

[1] Hann, R., and Johansen, T. A., "Unsettled Topics in Unmanned Aerial Vehicle Icing," *SAE Edge Report*, 2020. https://doi.org/10.4271/epr2020008.

[2] Shakhatreh, H., Sawalmeh, A. H., Al-Fuqaha, A., Dou, Z., Almaita, E., Khalil, I., Othman, N. S., Khreishah, A., and Guizani, M., "Unmanned aerial vehicles (UAVs): A survey on civil applications and key research challenges," *IEEE Access*, Vol. 7, 2019, pp. 48572–48634.

[3] Scalea, J. R., Restaino, S., Scassero, M., Blankenship, G., Bartlett, S. T., and Wereley, N., "An initial investigation of unmanned aircraft systems (UAS) and real-time organ status measurement for transporting human organs," *IEEE journal of translational engineering in health and medicine*, Vol. 6, 2018, pp. 1–7.

[4] Girard, A. R., Howell, A. S., and Hedrick, J. K., "Border patrol and surveillance missions using multiple unmanned air vehicles," *2004 43rd IEEE conference on decision and control (CDC)(IEEE Cat. No. 04CH37601)*, Vol. 1, IEEE, 2004, pp. 620–625.

[5] Hann, R., and Johansen, T. A., "UAV icing: the influence of airspeed and chord length on performance degradation," *Aircraft Engineering and Aerospace Technology*, Vol. 93, 2021, pp. 832–841. https://doi.org/10.1108/AEAT-06-2020-0127.

[6] Sørensen, K. L., Borup, K. T., Hann, R., Bernstein, B. C., and Hansbø, M., "Atmospheric icing limitations, climate report for Norway and surrounding regions," Tech. rep., UBIQ Aerospace, 2021.

[7] Bernstein, B. C., Wolff, C. A., and McDonough, F., "An inferred climatology of icing conditions aloft, including supercooled large drops. Part I: Canada and the continental United States," *Journal of applied meteorology and climatology*, Vol. 46, No. 11, 2007, pp. 1857–1878.

[8] Bernstein, B. C., and Le Bot, C., "An inferred climatology of icing conditions aloft, including supercooled large drops. Part II: Europe, Asia, and the globe," *Journal of applied meteorology and climatology*, Vol. 48, No. 8, 2009, pp. 1503–1526.

[9] Hann, R., Enache, A., Nielsen, M., Stovner, B., van Beeck, J., Johansen, T., and Borup, K., "Experimental Heat Loads for Electrothermal Anti-Icing and De-Icing on UAVs," *Aerospace*, Vol. 8, 2021, p. 83. https://doi.org/10.3390/aerospace8030083.

[10] Wallisch, J., and Hann, R., "UAV Icing: Experimental Investigation of Ice Shedding Times with an Electrothermal De-Icing System," *AIAA AVIATION 2022 FORUM*, 2022. (in press).

[11] Sørensen, K. L., Helland, A. S., and Johansen, T. A., "Carbon nanomaterial-based wing temperature control system for in-flight anti-icing and de-icing of unmanned aerial vehicles," *IEEE Aerospace Conference Proceedings*, Vol. 2015-June, 2015, pp. 1–6. https://doi.org/10.1109/AERO.2015.7119206.

[12] Sørensen, K. L., and Johansen, T. A., "Flight test results for autonomous icing protection solution for small unmanned aircraft," *2017 International Conference on Unmanned Aircraft Systems, ICUAS 2017*, Institute of Electrical and Electronics Engineers Inc., 2017, pp. 971–980. https://doi.org/10.1109/ICUAS.2017.7991301.

[13] Hann, R., Borup, K., Zolich, A., Sorensen, K., Vestad, H., Steinert, M., and Johansen, T., "Experimental investigations of an icing protection system for uavs," Tech. rep., SAE International, June 2019. https://doi.org/10.4271/2019-01-2038.

[14] Henry, R., "Development of an electrothermal de-icing/anti-icing model," *30th Aerospace Sciences Meeting & Exhibit*, AIAA 92-0526, 1992, p. 526. https://doi.org/10.2514/6.1992-526.

[15] Lei, G., Dong, W., Zhu, J., and Zheng, M., "A new melting model in electrothermal de-icing simulation," *Turbo Expo: Power for Land, Sea, and Air*, Vol. 56710, American Society of Mechanical Engineers, 2015, p. V05AT10A009.

[16] Enache, A., Bernay, B., Glabeke, G., Planquart, P., and van Beeck, J., "Ice shedding phenomenon: An experimental and numerical investigation," *AIAA AVIATION 2020 FORUM*, Vol. 1 PartF, 2020, p. 2817. https://doi.org/10.2514/6.2020-2817.

[17] Miller, R. H., and Larsen, M. L., "Optimal fault detection and isolation filters for flight vehicle performance monitoring," *IEEE Aerospace Conference Proceedings*, Vol. 7, 2003, pp. 3197–3203. https://doi.org/10.1109/AERO.2003.1234163.

[18] Sørensen, K. L., Blanke, M., and Johansen, T. A., "Diagnosis of wing icing through lift and drag coefficient change detection for small unmanned aircraft," *IFAC-PapersOnLine*, Vol. 28, 2015, pp. 541–546. https://doi.org/10.1016/j.ifacol.2015.09.582.

[19] Ding, D., Qian, W. Q., and Wang, Q., "Aircraft Inflight Icing Detection Based on Statistical Decision Theory," *IOP Conference Series: Materials Science and Engineering*, Vol. 751, IOP Publishing, 2020, p. 012054. https://doi.org/10.1088/1757-899X/751/1/012054, URL https://iopscience.iop.org/article/10.1088/1757-899X/751/1/012054https://iopscience.iop.org/article/10.1088/1757-899X/751/1/012054/meta.

[20] Hansen, S., and Blanke, M., "Diagnosis of airspeed measurement faults for unmanned aerial vehicles," *IEEE Transactions on Aerospace and Electronic Systems*, Vol. 50, No. 1, 2014, pp. 224–239. https://doi.org/10.1109/TAES.2013.120420.

[21] Du, P., Kibbe, W. A., and Lin, S. M., "Improved peak detection in mass spectrum by incorporating continuous wavelet transform-based pattern matching," *Bioinformatics*, Vol. 22, No. 17, 2006, pp. 2059–2065.

[22] Nenadic, Z., and Burdick, J. W., "Spike detection using the continuous wavelet transform," *IEEE transactions on Biomedical Engineering*, Vol. 52, No. 1, 2004, pp. 74–87.

[23] Zhang, Z.-M., Chen, S., and Liang, Y.-Z., "Peak alignment using wavelet pattern matching and differential evolution," *Talanta*, Vol. 83, No. 4, 2011, pp. 1108–1117. https://doi.org/https://doi.org/10.1016/j.talanta.2010.08.008, enhancing Chemical Separations with Chemometric Data Analysis.

[24] Sadowsky, J., "Investigation of signal characteristics using the continuous wavelet transform," *johns hopkins apl technical digest*, Vol. 17, No. 3, 1996, pp. 258–269.

[25] Tiihonen, M., Jokela, T., Makkonen, L., and Bluemink, G.-J., "VTT Icing wind tunnel 2.0," *Winterwind Presentations 2016*, 2016. Winterwind International Wind Energy Conference ; Conference date: 08-02-2016 Through 10-02-2016.

[26] Anderson, B., and Moore, J., *Optimal Filtering*, 1st ed., Dover Books on Electrical Engineering, Dover Publications, 2012. URL https://books.google.no/books?id=iYMqLQp49UMC.

[27] Matisko, P., and Havlena, V., "Optimality tests and adaptive Kalman filter," *IFAC Proceedings Volumes*, Vol. 45, No. 16, 2012, pp. 1523–1528. https://doi.org/https://doi.org/10.3182/20120711-3-BE-2027.00011, URL https://www.sciencedirect.com/science/article/pii/S1474667015381726, 16th IFAC Symposium on System Identification.

[28] The MathWorks, Inc., "fmincon," , 2022. URL https://se.mathworks.com/help/optim/ug/fmincon.html, (Accessed on 1/04/2022).

[29] Brown, R., *Introduction to random signals and applied Kalman filtering : with MATLAB exercises*, J. Wiley & Sons, Hoboken, NJ, 2012.

[30] Anderson, B., and Moore, J., *Optimal Filtering*, Prentice-Hall, 1979.

[31] Mallat, S. G., *A wavelet tour of signal processing*, 2nd ed., Academic Press, San Diego, 1999.

[32] The MathWorks, Inc., "Wavelet Toolbox," , 2022. URL https://www.mathworks.com/help/wavelet/index.html?s_tid=CRUX_lftnav, (Accessed on 1/04/2022).

[33] Olhede, S. C., and Walden, A. T., "Generalized morse wavelets," *IEEE Transactions on Signal Processing*, Vol. 50, No. 11, 2002, pp. 2661–2670.

[34] Lilly, J. M., and Olhede, S. C., "Higher-order properties of analytic wavelets," *IEEE Transactions on Signal Processing*, Vol. 57, No. 1, 2008, pp. 146–160.

[35] Zheng, D., Chao, B., Zhou, Y., and Yu, N., "Improvement of edge effect of the wavelet time–frequency spectrum: Application to the length-of-day series," *Journal of Geodesy*, Vol. 74, No. 2, 2000, pp. 249–254.

[36] Müller, N. C., Hann, R., and Johansen, T. A., "UAV Icing: A Performance Model for a UAV Propeller in Icing Conditions," *AIAA AVIATION 2022 FORUM*, 2022. (in press).